Optics Letters

Two-step spin coating $CsPbBr_3$ thin films and photodetectors in the atmosphere

Chenyang Bao, Xiang Peng, Leiying Ying, Yang Mei, Baoping Zhang, and Hao Long*

School of Electronic Science and Engineering (National Model Microelectronics College), Xiamen University, Xiamen, Fujian, 361005, China
**longhao@xmu.edu.cn*

Received 19 January 2023; revised 26 February 2023; accepted 28 March 2023; posted 29 March 2023; published 1 May 2023

Recently, inorganic halide perovskites, especially $CsPbBr_3$, have been attracting attention because of their high efficiency, wide color gamut, and narrow luminescent spectrum. To elevate the perovskite devices' performance, optimizations of crystalline quality, device structures, and fabrication process are essential. Currently, the state-of-the-art fabrication approach of $CsPbBr_3$ is spin-coating in an inert environment (nitrogen, argon, etc.), which requires temperature and humidity control. In this work, a $CsPbBr_3$-based visible photodetector (PD) is realized in a humid atmosphere, whose performances were comparable to those reported in an inert glovebox. The dependencies of responsivity and transient time on CsBr coating layer numbers and electrode period were also investigated. The best device performance was obtained with 4 layers of CsBr coating with a responsivity of 107.2 mA/W, detectivity of 4.29×10^{10} Jones, and quantum efficiency of 25.4%. The rise time of the 3–4-layer CsBr-coated PD was reduced by the higher crystalline quality and carrier mobility, while the decay time of the 1-layer CsBr-coated PD was faster since the dense defect induced non-radiative recombination centers. With the period T increasing, the responsivity decreased, while the transient times increased. We believe that our results could benefit the future optimization of perovskite materials and PDs.

https://doi.org/10.1364/OL.485858

Introduction. Recently, many opto-electronics (e.g., light-emitting diode, laser diode, solar cell, photodiode (PD), etc.) based on $CsPbBr_3$ have emerged, due to its high efficiency, wide color gamut, and narrow luminescent spectrum [1–6]. Among them, the $CsPbBr_3$ PD with high responsivity in the visible band is promising for application in the Internet of Things and underwater communication, because of its stability and strong dipole transition. In 2017, Liu's group achieved a 34-A/W $CsPbBr_3$ nanoflakes PD at 1.5 V by cation exchange [7]. High responsivity of 4.4×10^3 A/W and 0.252-ms transient time were also realized by a $CsPbBr_3$ nanowires PD [8]. To further enhance the device's properties, optimizations of crystalline quality and device design were required. Since halide perovskites degrade in air and moisture, spin-coating in an inert environment with strictly controlled temperature and humidity has been the most popular fabrication process for $CsPbBr_3$ materials and devices [9,10]. Conventionally, $CsPbBr_3$ materials have been synthesized in a nitrogen glovebox [11]. The reports about $CsPbBr_3$ materials synthesized in the atmosphere are rare. In 2021, Noh *et al*. reported a 9% photo-conversion efficient perovskite solar cell fabricated under a 40–50% relative humidity environment [12]. In 2020, Yang *et al*. assembled the $CsPbBr_3$ nanowires in the atmosphere [13]. Responsivity of 20 A/W and transient time of 0.3 ms were realized without observable degradation after 60 days air exposure. In 2022, Luo *et al*. [14] fabricated a stacked $CsPbBr_3$ PD in ambient air. Despite the above reports, the $CsPbBr_3$ thin films by spin coating in air have not been investigated in detail, and the device structures are still complex. Therefore, in this work, $CsPbBr_3$ thin films were spin-coated in a humid air condition by a two-step method. Metal-semiconductor-metal (MSM) PDs were fabricated on the $CsPbBr_3$ thin films with 1–6 CsBr layers. The effects of the number of CsBr layers on a thin film and PD were investigated. It was shown that the $CsPbBr_3$ PDs with 4 layers of CsBr yielded the best responsivity, detectivity, and quantum efficiency. The rise time of the PD was determined by the carrier mobility of $CsPbBr_3$, while the decay time of the PD was dominated by the recombination centers induced by defects. An increase of the electrode period rendered a lower responsivity and higher transient time.

Experiments. The $CsPbBr_3$ thin films were spin-coated in a 60% humidity, 25°C atmosphere. The Cr/Au (30/180 nm) interdigital electrodes were first deposited on a quartz substrate by photolithography and magnetron sputtering. All the electrode patterns maintained a 40% duty ratio (metal width/period) with periods ranging from 20 to 200 μm. A 1 M $PbBr_2$ solution (dissolved in DMF) was initially spin coated on the quartz substrate followed by 100°C, 45-min thermal annealing in the atmosphere. Respectively 1–6 layers of 0.07 M CsBr (in CH_3OH) solution were then deposited on the annealed $PbBr_2$ layer to form the $CsPbBr_3$ thin films, as illustrated in Fig. 1.

X ray diffraction (XRD) 2θ–ω phase analysis scattering was performed by TD-3500 XRD apparatus. Scanning electron microscopy (SEM) images were taken by a Carl Zeiss Sigma-HD microscope. The surface morphology and thicknesses of the perovskites were detected by a stepper profiler (Bruker Dektak-XT). The dark and photo current–voltage curves of the perovskite PD were measured by a Keithley 2450 source meter, with a 10-mW/cm^2, 525-nm LED excitation source.

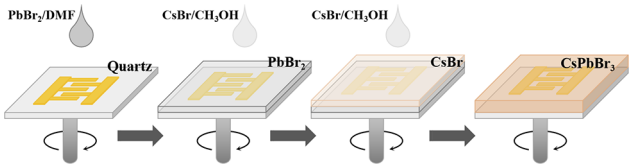

Fig. 1. Two-step spin coating of perovskite.

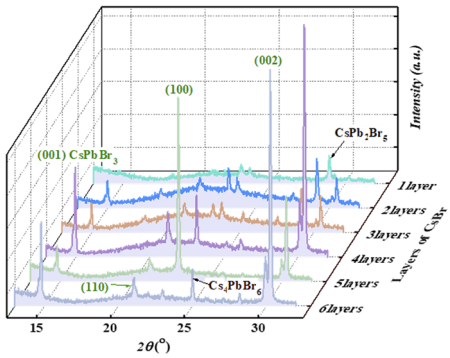

Fig. 2. XRD 2θ–ω of $CsPbBr_3$ with different layer numbers of CsBr.

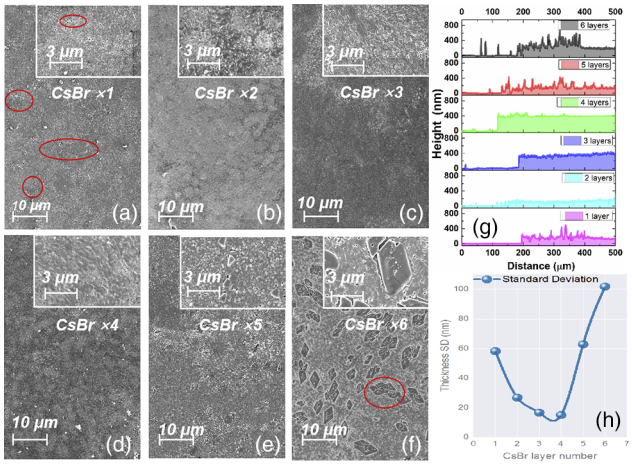

Fig. 3. (a)–(f) SEM images of $CsPbBr_3$ thin films with 1–6 layers of CsBr, (g) perovskite stepper profile, and (h) SD of morphology.

Results and discussion. Figure 2 shows that the perovskite with different CsBr layer number typically exhibited (001), (002), and (100) planes of $CsPbBr_3$. Perovskite with 1–2 layers of CsBr also had the $CsPb_2Br_5$ phase, which meant unconsumed $PbBr_2$, while the 6 layers of CsBr formed Cs_4PbBr_6, which represented excess CsBr content. Our results coincided with other two-step spin coatings in an inert environment [3].

Figures 3(a)–3(f) represent the SEM images of 1–6-layer CsBr-coated $CsPbBr_3$ thin films. All the thin films exhibited good surface coverage, which was ascribed to the annealing of $PbBr_2$. Under high magnification, some nano voids could be observed in the perovskite with only one layer of CsBr [Fig. 3(a)]. With increasing the number of CsBr layers, the voids disappeared by the growth of the crystal grain. No voids were detected in the 3–4-layer CsBr-coated sample. When the CsBr coating number was further increased, the grains merged with each other by recrystallization. Some crystal bulks with

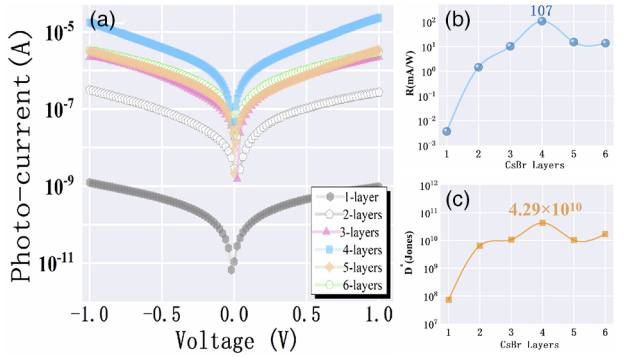

Fig. 4. (a) Photo-induced *I*–*V*, (b) responsivity, and (c) detectivity with different numbers of CsBr layers.

tens of micrometers were shown in the 5–6-layer CsBr coating [Figs. 3(e) and 3(f)], along with voids on the grain boundary. Figures 3(g) and 3(h) show the profile and standard deviation (SD) of perovskites. With increasing the CsBr content, the thickness of $CsPbBr_3$ increased from 120 nm of 2-layer CsBr to 400 nm of 3–4 layers, and then became saturated. The surface morphology was also smooth for 3–4-layers CsBr with less than 20-nm SD. With insufficient or excessive CsBr, the morphology became rough, which was also in line with the SEM images. The lowest trap density of 2.13×10^{13} cm^{-3} by the space-charge limited current (SCLC) model [14] and the highest photoluminescent quantum yield (PLQY) were also obtained with the 4-layer CsBr coating (not shown), confirming the best quality of the 4-layer CsBr sample.

The −1 to 1 V photo current–voltage curves of 1–6-layer CsBr coating $CsPbBr_3$ PD with 20-μm period were measured, as shown in Fig. 4(a). All curves represented symmetrical Schottky contact. Highest photo current appeared for the 4-layer CsBr-coated sample. This could be explained by the high absorption coefficient and mobility of 4-layer CsBr perovskite.

The responsivity R and detectivity D^* are defined as

$$R = \frac{I_L - I_d}{P \times S} \text{ and } D^* = \frac{R\sqrt{Sf}}{I_n} = \frac{R\sqrt{S}}{\sqrt{2eI_d}};$$

where $I_L, I_d, P, S, f, I_n, e$ represent the photocurrent, dark current, incident light power, illumination area, cutoff frequency, noise current, and electron charge, respectively [15]. Both R and D^* were averaged by several samples with 5% variance. Figures 4(b) and 4(c) show that the responsivity and detectivity achieved the maximal values of 107 mA/W and 4.29×10^{10} Jones for the 4-layer CsBr perovskite, corresponding to a quantum efficiency of 25.4%. This should also be ascribed to the smooth surface, pure crystal phase, compact grains, and higher crystalline quality of 4-layer CsBr-coated $CsPbBr_3$. Although synthesized under a humid atmosphere, our $CsPbBr_3$ PD exhibited comparable performance with those fabricated in an inert environment (e.g., 200 mA/W of Lai's thin film PD) [6,16–20].

As shown in Fig. 5(a) and its enlarged inset, the $CsPbBr_3$ PD repeated well after cycles. Figure 5(b) shows that the rise time τ_r presented an opposite trend with CsBr layer numbers to the decay time τ_d. The rise time had a minimum of approximately 223.8 ms at 3–4 layers CsBr, while the decay time achieved a maximum at 3–5-layers CsBr. To explain this phenomenon, a transient model was proposed. The rise time was determined by two processes: the RC time constant τ_{rc} and the carrier transit

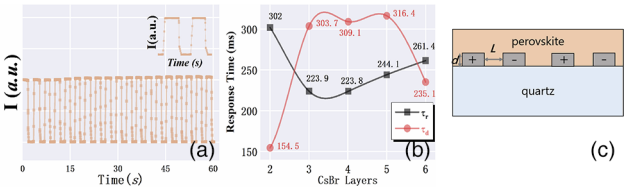

Fig. 5. (a) Repeated PD responsive curve, (b) rise and decay times of PD with different CsBr layer numbers, and (c) schematic interdigital electrode structure of MSM PD.

time τ_{tr}: $\tau_r^{-1} = \tau_{rc}^{-1} + \tau_{tr}^{-1}$. As shown in Fig. 5(c), the parallel capacity of MSM interdigital structure was

$$C = \frac{dl\varepsilon_0\varepsilon_i}{L}n, \tag{1}$$

where d is the electrode thickness; l is the electrode length; L is the effective interval of electrode in single period; and ε_0 and ε_i are the dielectric coefficients of vacuum and perovskite. Similarly, the parallel resistance should be

$$R = \rho\frac{L}{d\cdot l}\cdot\frac{1}{n}. \tag{2}$$

The RC time constant is

$$\tau_{rc} = RC = \varepsilon_0\varepsilon_i\rho = \frac{\varepsilon_0\varepsilon_i}{n_e q\mu}, \tag{3}$$

where n_e, q, μ are the carrier concentration, electron charge, and mobility, respectively. The carrier transit time τ_{tr} was determined by the L and electrode velocity v_s: $\tau_{tr} = L/v_s$. The velocity of electron was related with the mobility μ and electric field E: $v_s = \mu\cdot E$. The electric field could be estimated by the voltage U and L. Therefore, the transit time is

$$\tau_{tr} = \frac{L^2}{\mu\cdot U}. \tag{4}$$

The rise time follows

$$\tau_r^{-1} = \tau_{rc}^{-1} + \tau_{tr}^{-1} = \left(\frac{\varepsilon_0\varepsilon_i}{n_e q\mu}\right)^{-1} + \left(\frac{L^2}{\mu\cdot U}\right)^{-1}. \tag{5}$$

Because the $CsPbBr_3$ materials with 3–4-layers CsBr exhibited a better crystalline quality with higher carrier mobility, the rise process of these two PDs were thus swift, which coincided with the experimental results [Fig. 5(b)]. With increasing or decreasing the CsBr layer number, voids and fluctuations appeared at the grain boundaries and surface (Fig. 2), the carrier mobility and crystal quality decayed, prolonging the rise time.

However, during the decay process, in addition to the RC constant and transit time, the recombination process by defects dominated. Since our perovskite was spin-coated by solution, the polycrystalline phase of $CsPbBr_3$ was confirmed by XRD phase analysis and SEM. Defects in grains and along the grain boundary were believed to play a role as non-radiative recombination centers. When excess carriers were generated by photon illumination, most carriers should be annihilated through defect assisted recombination. Therefore, the decay time τ_d was expressed by

$$\tau_d^{-1} = \tau_{rc}^{-1} + \tau_{tr}^{-1} + \tau_{nr}^{-1} = \left(\frac{\varepsilon_0\varepsilon_i}{n_e q\mu}\right)^{-1} + \left(\frac{L^2}{\mu\cdot U}\right)^{-1} + k\rho_D, \tag{6}$$

where the non-radiative recombination rate was proportional to the defect density ρ_D: $\tau_{nr}^{-1} = k\cdot\rho_D$. Since the defect density was

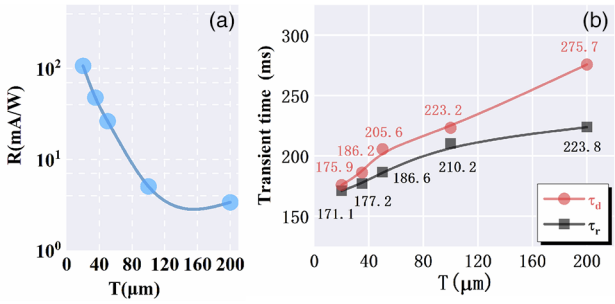

Fig. 6. (a) Responsivity and (b) transient time of 4-layer CsBr-coated perovskite PDs with different electrode period.

higher in 2- and 5–6-layers CsBr perovskite, the decay times of these PDs were thus faster than the 3–4-layers CsBr PD.

The effect of electrode period T on the perovskite PD's performance was also investigated. Figure 6 shows the responsivities and transient times of PDs with 40% duty ratio and different period from 20–200 μm. By increasing the period, the PD's responsivity decreased. This could be ascribed to the increase of resistance ($R = \frac{\rho L}{Wln} = \frac{3\rho T}{2lD}$, where D is the whole length of the PDs), and reduction of the effective electric field ($E = U/L$) by elongating the electrode intervals.

Figure 6(b) shows that the rise and decay processes were both delayed by increasing the period. In Fig. 5(c), the intervals L between anode and cathode could be expressed as $L = 0.6\,T$ (40% duty ratio). Equations (5) and (6) are transformed into

$$\tau_r^{-1} = \left(\frac{\varepsilon_0\varepsilon_i}{n_e q\mu}\right)^{-1} + \left(\frac{0.36T^2}{\mu\cdot U}\right)^{-1}, \tag{7}$$

$$\tau_d^{-1} = \left(\frac{\varepsilon_0\varepsilon_i}{n_e q\mu}\right)^{-1} + \left(\frac{0.36T^2}{\mu\cdot U}\right)^{-1} + k\rho_D. \tag{8}$$

The period T affected the transit time τ_{tr} through carrier velocity v_s ($= \mu E$), which was inversely proportional to the period T at same voltage U. Therefore, the transit times τ_r and τ_d both increased with period T, following the second terms of Eqs. (7) and (8), which coincided with experiments.

Conclusion. In this work, $CsPbBr_3$ materials and PD devices were spin-coated in a humid atmosphere, showing comparable performance to those synthesized in an inert environment. The 4-layer CsBr-coated $CsPbBr_3$ thin films exhibited the best crystalline quality and compact surface. The PD based on the 4-layer CsBr-coated $CsPbBr_3$ thin film yielded the best performance of a responsivity of 107.2 mA/W, quantum efficiency of 25.4%, and detectivity of 4.29×10^{10} Jones. The carrier mobility and defect density determined the rise and decay time, respectively, rendering the fastest rise and slowest decay time for the 3–4-layers CsBr-coated perovskite. The effect of electrode period on PD performance was also investigated, showing that the responsivity decreased while transient time increased with the period.

Funding. National Natural Science Foundation of China (62174140); Youth Innovation Foundation of Xiamen, China (3502Z20206055); Fundamental Research Funds for the Central Universities (20720220077).

Disclosures. The authors declare no conflicts of interest.

Data availability. Data underlying the results presented in this paper are not publicly available at this time but may be obtained from the authors upon reasonable request.

REFERENCES

1. L. Protesescu, S. Yakunin, I. Bodnarchuk M, F. Krieg, R. Caputo, H. Hendon C, X. Yang R, A. Walsh, and V. Kovalenko M, Nano Lett. **15**, 3692 (2015).
2. D. J. Wu, Y. C. Xu, H. Zhou, X. Feng, J. Q. Zhang, X. Y. Pan, Z. Gao, R. Wang, G. K. Ma, L. Tao, H. B. Wang, J. X. Duan, H. Z. Wan, J. Zhang, L. P. Shen, H. Wang, and T. Y. Zhai, InfoMat **4**, e12320 (2022).
3. J. F. Zheng, Y. J. Wu, Y. J. Sun, J. H. Rong, H. Y. Li, and L. Niu, Nano-Micro Lett. **13**, 1 (2020).
4. Z. Gao, H. Zhou, K. L. Dong, C. Wang, J. Y. Wei, Z. Li, J. S. Li, Y. J. Liu, J. Zhao, and G. J. Fang, Nano-Micro Lett. **14**, 215 (2022).
5. K. Lin, J. Xing, L. Quan, F. P. G. Arquer, X. Gong, J. Lu, L. Xie, W. Zhao, D. Zhang, C. Yan, W. Li, X. Liu, Y. Lu, J. Kirman, E. H. Sargent, Q. Xiong, and Z. Wei, Nature **562**, 245 (2018).
6. Z. X. Lai, Y. Meng, F. Wang, X. M. Bu, W. Wang, P. S. Xie, W. J. Wang, C. T. Liu, S. P. Yip, and J. C. Ho, Nano Res. **15**, 3621 (2022).
7. X. H. Liu, D. J. Yu, F. Cao, X. M. Li, J. P. Ji, J. Chen, X. F. Song, and H. B. Zeng, Advanced Science News **13**, 1700364 (2017).
8. M. Shoaib, X. Zhang, X. Wang, H. Zhou, T. Xu, X. Wang, X. Hu, H. Liu, X. Fan, and W. J. Zheng, J. Am. Chem. Soc. **139**, 15592 (2017).
9. A. R. Pascoe, Q. Y. Gu, M. U. Rothmann, W. Li, and Y. B. Cheng, Sci. China Mater. **60**, 617 (2017).
10. J. H. Im, I. H. Jang, N. Pellet, M. Gritzel, and N. G. Park, Nat. Nanotechnol. **9**, 927 (2014).
11. X. Wan, Z. Yu, W. Tian, F. Huang, S. Jin, X. Yang, Y. B. Cheng, A. Hagfeldt, and L. Sun, J. Energy Chem. **46**, 8 (2020).
12. M. F. M. Noh, N. A. Arzaee, I. N. N. Mumthas, A. Aadenan, and M. A. M. Teridi, Opt. Mater. **118**, 111288 (2021).
13. Y. Q. Yang, F. L. Gao, Q. Liu, J. Q. Dong, D. Y. Li, X. J. Luo, J. Q. Guo, J. Shi, Y. L. Lin, W. D. Song, X. F. Wang, and S. T. Li, J. Phys. Chem. Lett. **11**, 7224 (2020).
14. M. M. Luo, S. K. Yan, C. T. Wei, X. Lu, C. J. Liu, O. E. Fayemi, B. S. Bae, S. B. Shafie, M. Xiao, Q. Li, Z. W. Zhao, J. Wu, W. Lei, and X. B. Zhang, Adv. Mater. Interfaces **9**, 2200450 (2022).
15. K. L. Dong, H. Zhou, W. L. Shao, Z. Gao, F. Yao, M. Xiao, J. H. Li, Y. J. Liu, S. X. Wang, S. Zhou, H. S. Cui, M. C. Qin, X. H. Lu, C. Tao, W. J. Ke, and G. J. Fang, ACS Nano **17**, 1495 (2023).
16. J. P. Zeng, C. F. Meng, X. M. Li, Y. Wu, S. T. Liu, H. Zhou, H. Wang, and H. B. Zeng, Adv. Funct. Mater. **29**, 1904461 (2019).
17. F. R. Cao, W. Tian, K. M. Demg, M. Wamg, and L. Li, Adv. Funct. Mater. **29**, 1906756 (2019).
18. P. B. Gui, J. S. Li, X. L. Zheng, H. B. Wang, F. Yao, X. Z. Hu, Y. J. Liu, and G. J. Fang, J. Mater. Chem. C **8**, 6804 (2020).
19. Z. Y. L. Zhang, W. T. Zhang, Z. M. Wei, Q. B. Jiang, M. Y. Deng, W. M. Chai, W. D. Zhu, C. F. Zhang, H. L. You, and J. C. Zhang, Sol. Energy **209**, 371 (2020).
20. G. B. Gen, Y. J. Liu, C. X. Zhao, G. Wang, Y. Fu, G. H. Yan, Y. Yuan, C. H. Su, Z. J. Zhao, and W. J. Mai, Small **15**, 1902135 (2019).